Climate control on Early Cenozoic denudation of the Namibian margin as deduced from new thermochronological constraints

Audrey Margirier[1,2,3,*], Jean Braun[1,2], Cécile Gautheron[4], Julien Carcaillet[5], Stéphane Schwartz[5], Rosella Pinna Jamme[4], Jessica Stanley[1, 6]

[1] Helmholtz Centre Potsdam, GFZ German Research Center for Geosciences, Telegrafenberg Building A27, 14473 Potsdam, Germany.

[2] Now at the Institut für Erd- und Umweltwissenschaften, Universität Potsdam, 14476 Potsdam, Germany

[3] Department of Geosciences, University of Arizona, 1040 East 4th St., Tucson, Arizona, 85721 USA.

[4] GEOPS, Univ. Paris-Sud, CNRS, Université Paris-Saclay, 91405 Orsay, France.

[5] ISTerre, Univ. Grenoble Alpes, Univ. Savoie Mont Blanc, CNRS, IRD, IFSTTAR, 38000 Grenoble, France.

[6] Now at the Department of Geological Sciences, University of Idaho, Moscow, Idaho, USA.

* Corresponding author, audrey.margirier@gmail.com

Abstract

The processes that control long term landscape evolution in continental interiors and, in particular, along passive margins such as in southern Africa, are still the subject of much debate (e.g. Braun, 2018). Although today the Namibian margin is characterized by an arid climate, it has experienced climatic fluctuations during the Cenozoic and, yet, to date no study has documented the potential role of climate on its erosion history. In western Namibia, the Brandberg Massif, an erosional remnant or inselberg, provides a good opportunity to document the Cenozoic denudation history of the margin using the relationship between rock cooling or exhumation ages and their elevation. Here we provide new apatite (U-Th-Sm)/He dates on the Brandberg Inselberg that range from 151±12 to 30±2 Ma. Combined with existing apatite fission track data, they yield new constraints on the denudation history of the margin. These data document two main cooling phases since continental break-up 130 Myr ago, a rapid one (~10°C/Myr) following break-up and a slower one (~1-2°C/Myr) between 65 and 35 Ma. We interpret them respectively to be related to escarpment erosion following rifting and continental break-up and as a phase of enhanced denudation during the Early Eocene Climatic Optimum. We propose that during the Early Eocene Climatic Optimum chemical weathering was important and contributed significantly to the denudation of the Namibian margin and the formation of a pediplain around the Brandberg and enhanced valley incision within the massif. Additionally, aridification of the region since 35 Ma has resulted in negligible denudation rates since that time.

Keywords

Climate, Early Eocene Climatic Optimum, thermochronology, apatite (U-Th-Sm)/He, denudation, weathering, Namibian passive margin

1. Introduction

The surface of the Earth's continents is shaped by complex interactions between tectonics and climate. The combined effects of tectonics and erosion on continental topography have been studied for a long time in convergent settings (e.g. Willett, 1999; Whipple, 2009). However, the role of climate in cratonic areas and, in particular, in the vicinity of passive margins is not well documented due to the low erosion rate and relative stability of the landscape. In southern Africa, the landscape of the Atlantic margin is thought to be inherited from rifting and continental break-up 130 Myr ago (e.g. Brown et al., 1990; Dauteuil et al., 2013; Brown et al., 2014; Brune et al., 2016; Wildman et al. 2016; Wildman et al., 2019) and is mostly considered stable over time scales $<10^6$ yrs (e.g. Cockburn et al., 2000; Matmon et al., 2018). Several studies focused on denudation have aimed to better constrain the topographic evolution of the passive margin. Apatite fission track studies document a post-rift cooling phase at ~80-70 Ma, which, combined with structural evidence from the adjacent offshore Walvis Basin, is interpreted as evidence a late episode of uplift along the margin associated with the reactivation of inherited tectonic lineaments (Raab et al., 2002; Raab et al., 2005; Brown et al., 2014). However, the late denudation history (<70 Ma) is not well constrained and the impact of climate on Cenozoic denudation history has never been considered even though the Namibian margin was subject to strong climate variations during the Cenozoic, as evidenced from laterite formation during the Late Paleocene Thermal Maximum and Early Eocene Climatic Optimum (Pickford and Senut, 1999; Zachos et al., 2001; Pickford et al., 2014), followed by a rapid aridification during the middle Eocene and a present day arid climate (Scott et al., 2006; Pickford et al., 2014).

Today the Namibian margin is characterized by very slow erosion of a granitic landscape (<5 m.Ma^{-1}, Cockburn et al., 2000; Matmon et al., 2018). The topography of the margin is

characterized by an escarpment, located 200 km away from the coast, separating low elevation pediplain from a high elevation plateau, the Kalahari or South African Plateau (Fig. 1A, 1B). The pediplains form a dry, flat and rocky landscape which is studded with numerous inselbergs (Fig. 1A). The high topographic relief of these inselbergs makes them ideal targets for quantifying the denudation history of the area using low-temperature thermochronology because they provide an opportunity to compare rock cooling histories from a range of elevations. Furthermore, the use of two thermochronological systems with different thermal sensitivities provides additional constraints on the thermal and thus erosional history of the area. Consequently, we focused our study on the Brandberg Massif (Fig. 1), one of the largest and tallest inselberg along the Namibian margin where we performed a thermochronological study combining new apatite (U-Th-Sm)/He (AHe) dates and published apatite fission track (AFT) data in order to constrain the thermal and denudation history of the Namibian margin since continental breakup.

2. Geological and geomorphological setting

2.1 Geology and geomorphology of the Namibian margin

The Namibian margin was formed following rifting and continental break-up 130 Ma ago (Brune et al., 2016; Baby et al., 2018), during the opening of the South Atlantic Ocean where sea-floor spreading initiated at the time of magnetic anomaly M3 (Gradstein et al, 2012). Rifting is likely to have led to uplift of the margin creating the great escarpment (Gallagher and Brown, 1999). The basement of central Namibia consists of Proterozoic rocks (2.1 – 1.7 Ga) that represent the southernmost extent of the Congo Craton (Fig. 1A). The basement is bounded to the west and to the south by a continental scale shear zone trending NE-SW inherited from the Pan-African Damara

orogeny, which is intruded by granitoids of Damara age (Fig. 1A; Miller, 1983). Basement is partially covered by meta-sedimentary rocks including the Neoproterozoic Damara Sequence and the Permian to Jurassic Karoo Sequence and by Early Cretaceous Etendeka flood basalts (132-127 Ma; ^{40}Ar-^{39}Ar; e.g. Renne et al., 1996; Stewart et al., 1996). These volcanic rocks can reach a thickness of 3 km (Milner et al., 1995; Baby, 2017). Measurements of magnetic susceptibility anisotropy suggest that the Etendeka flood basalts emplaced soon after the initiation of rifting and were controlled by rift related topographic features (e.g. Glen et al., 1997). Numerous Early Cretaceous magmatic intrusions, dikes and sills intrude the basement, the Karoo sedimentary rocks and the overlying lavas (Fig. 1A; Trumbull et al., 2004). These intrusions emplaced as subvolcanic complexes at shallow levels in the crust (Diehl, 1990) shortly after eruption of the Etendeka flood basalts. All these Early Cretaceous intrusions are distributed along a northeast trending zone which corresponds to the Damara Orogen (Fig. 1A). Today they form characteristic topographic features of the north western Namibian landscape. Among them, the Brandberg Inselberg represents the highest peak of Namibia. It forms an isolated massif of 25 km diameter, culminating at 2573 m above sea level and rising 1500 m above the surrounding pediplains (Fig. 1B, C). Geologic constraints and K-Ar and ^{40}Ar-^{39}Ar dating (Schmitt et al., 2000 and references therein) indicate that the Brandberg was emplaced at 132-130 Ma at shallow depth in the Damara sequence and Etendeka basalts.

2.2 Denudation history of the Namibian margin inferred from low-temperature thermochronology

Previous studies have provided low-temperature thermochronological data (apatite fission track and (U-Th-Sm)/He) from the Kalahari Plateau to document its long-term

120 denudation history (e.g. Raab et al., 2005; Brown et al., 2014; Stanley et al., 2015;
121 Wildman et al., 2017). Along southern Africa passive margins, several studies produced
122 apatite fission track (AFT) data seaward from the escarpment (Fig. 1A; e.g. Haack et al.,
123 1983; Brown et al., 1990; Gallagher and Brown, 1999; Raab et al., 2002; 2005; Tinker et
124 al., 2008; Brown et al., 2014; Wildman et al., 2016; Wildman et al., 2019). In Namibia the
125 AFT data suggest that rocks located in the Brandberg area have been exposed to high
126 temperatures (> 120°C, to reset fission tracks) during the Etendeka magmatic episode
127 that caused thermal annealing of preexisting fission tracks (Brown et al., 2014). In
128 contrast with other passive margins, there is no clear gradient in AFT dates across the
129 Namibian great escarpment (Haack, 1983; Brown et al., 1990; Gallagher and Brown,
130 1999; Raab et al., 2002; 2005; Brown et al., 2014). Based on this absence of gradient,
131 Brown et al. (1990) proposed uniform erosion of 3 km across the escarpment during the
132 Early Cretaceous. This value is likely to be underestimated for the Brandberg region
133 where AFT data and thermal modelling suggest that total erosion since continental
134 break-up is likely to reach ~5 km (Raab et al., 2005). Based on AFT data and associated
135 thermal modelling, different exhumation phases have been identified along the
136 Namibian margin: several studies identified a first denudation phase during the Early
137 Cretaceous and suggest that it could be related to enhanced denudation following
138 continental break-up (Brown, 1990; Gallagher and Brown, 1999; Brown, 2014); another
139 major denudation phase has been identified in several places along the Namibian
140 margin from ~90-70 Ma to ~70-60 Ma (Raab et al., 2002; 2005; Brown et al., 2014)
141 potentially related to post break-up reactivation of the Damara shear zone (Raab et al.,
142 2002; Brown et al., 2014) or a more recent (Late Cretaceous) regional uplift of the entire
143 Kalahari Plateau (e.g. Rouby et al, 2009). In the context of the low denudation rates in

Namibia the thermal sensitivity of AFT thermochronological system did not allow to constrain the recent (<60 Ma) cooling and denudation history.

3. Low-temperature thermochronology

Low-temperature thermochronology provides information on cooling histories that can be related to local exhumation processes.

3.1 Apatite fission-track data

3.1.1 Basics of apatite fission track dating

The fission track method is based on the accumulation of small damages known as fission tracks in uranium rich minerals which form during the spontaneous radioactive decay of 238 U (e.g. Gleadow and Brown, 2000). If the mineral is subjected to high temperatures, fission tracks that already formed will anneal and ultimately be erased. The fission track length depends on heating duration and temperature, and the annealing temperature varies among minerals. Furthermore, AFT age can also decrease due to an auto annealing process (e.g. Green, 1988; Brown et al., 1990) that is particularly observed in long, protracted cooling histories. Apatite FT age and tracks lengths record rock cooling history from temperature ranging from 110 to 60°C (e.g. Gallagher et al., 1998). Considering a surface mean temperature of 20°C and geothermal gradient of 20°C/km (a reasonable value for a cratonic area) it can therefore record erosion over a 5-2 km depth range. AFT can also record reheating of the crust due to burial or an extensive volcanic event (see, for example, Gleadow and Brown, 2000).

3.1.1 Existing apatite fission track data

Raab et al. (2005) provided AFT dates and lengths for 11 samples from the southern flank of the Brandberg. The AFT dates are correlated with elevation with older dates obtained at higher elevations. They range from 98 ± 9 Ma at the top of the Brandberg massif to 69 ± 4 Ma at the base of the Hongorob Valley. The mean track-length varies from 15.1 ± 0.4 μm to 12.2 ± 1.1 μm (Raab et al., 2005).

3.2 Apatite (U-Th-Sm)/He data

3.2.1 Basics of apatite (U-Th-Sm)/He dating

(U-Th-Sm)/He thermochronology is based on the accumulation of ^{4}He produced by the radioactive decay of ^{238}U, ^{235}U, ^{232}Th, and ^{147}Sm in rocks and minerals over time. Although ^{4}He is produced continuously by alpha decay, at high temperatures He diffuse rapidly out of the mineral of interest. Conversely, once a mineral is cool enough, He atoms are retained in the crystal. The apatite (U-Th-Sm)/He (AHe) thermochronological system records temperature evolution from 120 to 30°C (Djimbi et al., 2015; Gautheron et al., 2009; Flowers et al., 2009). Natural radiation damage created in the crystal over geologic time-scale increases the ^{4}He retentivity in apatite, so the closure temperature increases as damage is produced by U and Th decay. Thus, for apatite crystals that stayed a long time in the partial retention zone (i.e., between 120 and 30°C), a positive correlation between AHe dates and effective uranium eU (U+0.24Th) has been observed (e.g. Flowers and Kelley, 2011). This reflects the damage accumulation with time and effective uranium content. From a physical point of view, He atoms are blocked within damages and require more energy to go back into the crystal lattice (Shuster et al., 2006). Two He diffusion models propose that the trapping energy is constant with damage concentration (Gautheron et al., 2009; Flowers et al., 2009), whereas a third, more recent model proposes that the trapping energy increases with damage

concentration until it reaches a percolation threshold (Gerin et al., 2017). In cratonic areas and passive margin environments, characterized by long and protracted thermal histories, it has been shown that the Gautheron et al. (2009) and Flowers et al. (2009) diffusion models fail to reproduce simultaneously AFT and AHe data (Wildman et al., 2016; Jess et al., 2018; Recanati et al., 2017). The Gerin et al. (2017) diffusion model was recently tested and calibrated by Recanati et al. (2017) who propose a trapping energy increase of 30 to 70 kJ/mol. The Gerin et al (2017) model makes it possible to exploit the dispersion in the AHe dates to reconstruct the thermal history through the partial retention zone. Apatite chemistry (Gautheron et al., 2013), small voids (Zeitler et al., 2017) and crystal size and fragmentation (e.g. Brown et al., 2013) also affect AHe dates and a correction must be made for He ejected from the crystal as it is produced due to long alpha particle stopping distances (Ketcham et al., 2011). Note that all the figures show non corrected AHe dates to be consistent with dates predicted by thermal modelling.

3.2.2 Sampling strategy: vertical profile

Thermochronological age–elevation relationships can be used to better constrain the rate of rock exhumation (e.g. Gleadow and Fitzgerald, 1987). The Brandberg Inselberg with its ~2000 m of relief gives the best opportunity to sample a vertical profile on the Namibian margin. We sampled a vertical profile in the Brandberg Inselberg (Hungorob Valley) with elevation ranging from 600 to 1800 m for AHe dating. We also sampled at the bottom of the Tsisab Valley (600 m asl) and 17 km east of the Brandberg Inselberg in the pediplain (780 m asl; Fig. 1).

3.2.3 Apatite (U-Th-Sm)/He: data and results

This study provides 25 new single-grain apatite (U-Th-Sm)/He dates for 4 samples along a vertical profile in the Brandberg Massif and one in the pediplain (4 to 7 crystals dated per sample; Table 1; details on sample processing, and analysis are provided in the Supplements). The single grain dates obtained from the pediplain range from 128±10 to 72±6 Ma. The dates in the Brandberg Inselberg range from 151±12 to 30±2 Ma (Table 1; Fig. 2) and show a clear positive age-elevation relationship. The dates obtained from the lowest sample (sample NAM14-08; eastern part of the Brandberg Inselberg) range from 66±5 to 30±2 Ma. By contrast, the samples located at higher elevation (1387-1769 m asl), show older apatite (U-Th-Sm)/He dates ranging from 151±12 to 74±6 Ma. The effective uranium concentration of the apatite crystals ranges from very low to intermediate value, i.e. 1 to 51 ppm. The observed date dispersion observed for most of the samples is correlated with the effective uranium concentration (Fig. 2B). The NAM14-11F single-grain AHe date of 140±11Ma (eU = 1 ppm) might be affected by ^{4}He implantation due to rich U-Th neighbor minerals (Murray et al., 2014; this grain is represented in pastel on Fig. 2). Most of the AHe dates (151±12 to 74±6 Ma) from the Brandberg Massif are older than AFT dates (98±9 to 68±12 Ma; Raab et al., 2005) obtained in the same area and at the same elevation except for the sample located at the lowest elevation (NAM14-08; Fig. 4A; Table 1). Together with the AFT dates and track lengths collected by Raab et al. (2005) in the Brandberg, our AHe dates ranging from 151±12 to 30±2 Ma provides constraints on the thermal history of the Brandberg from 120 to 30°C (e.g. Djimibi et al., 2015; Gallagher et al., 1998; Gautheron et al., 2009; Flowers et al., 2009).

4. Thermal history modelling

4.1 Thermal modelling principle and setup

Thermal histories for the Brandberg vertical profile were determined using QTQt, a piece of software that inverts AFT annealing and AHe diffusion parameters using a Markov chain Monte Carlo method (Gallagher, 2012 and references therein). The input data used for the thermal modelling are the central AFT dates and the track length distributions produced by Raab et al. (2005) and our single-grain AHe dates with their diffusion domain size (sphere equivalent radius for each apatite crystal) and chemical characteristics (U-Th-Sm content; this study). We excluded the NAM14-11A single-grain AHe date from our modelling because we suspect the nearby presence of a U-Th rich inclusion (Table 1). We used the multi-kinetic annealing model of Ketcham et al. (2007) to model the AFT dates and track-length dispersion. For the AHe dates, the grain chemical composition range can be taken into consideration following Gautheron et al. (2013). Because the high elevation samples have a significant residence time above the partial retention zone, we took into account the potentially large volume of accumulated defaults in apatite crystals to explain the old AHe dates. We performed simulations using the linear (Gautheron et al., 2009) and non-linear He damage models (Flowers et al., 2009), as well as the new radiation damage diffusion model proposed by Gerin et al. (2017). For this we used activation energy values in agreement with those proposed by Recanati et al. (2017): respectively, 30-50, 60, 60 and 70 kJ/mol for samples NAM14-08 (639 m asl), NAM14-11 (1387 m asl), NAM14-10 (1433 m asl) and NAM14-09 (1769 m asl) in agreement with fission track density variation with elevation within the Brandberg Massif (Raab et al., 2005; Gerin et al., 2017; Recanati et al., 2017).

Initial conditions for the model are fixed at t = 120 ± 10 Ma and T = 300 ± 50°C based on ^{40}Ar-^{39}Ar cooling dates (132-130 Ma; Schmitt et al., 2000). In the model the present day temperature is fixed at 10°C for the highest sample of the profile at 2573 m asl (Raab et al., 2005) and the atmospheric gradient is fixed at 6.5°C.km^{-1}. The thermal history

simulations are the product of 200,000 iterations, which is here a sufficient amount to obtain stable solutions (e.g. Gallagher, 2012).

4.2 Time-temperature inversion results

The long thermal history of our samples and date-eU correlations observed in our data suggest that radiation damage controls the He diffusivity of the apatites and must be taken into account. The choice of radiation damage accumulation and annealing model can have an important control on the thermal history inversion results. Initially, we tried simulating the data with the more established Gautheron et al. (2009) and Flowers et al. (2009) He radiation damage models. The QTQt simulations using these models predict similar thermal histories for all samples in the Brandberg Massif (Figure 3). However, the thermochronological dates predicted by these simulations fail to reproduce both the AFT and AHe dates of the Brandberg profile. Specifically, the relatively old AHe dates of the samples NAM14-09, NAM14-10 and NAM14-11 are not reproduced by the simulations using either of these radiation damage models (Fig 3A, C).

To address this discrepancy, we performed a thermal history simulation using the more recent radiation damage model of Gerin et al. (2017) and the activation energy values proposed by Recanati et al. (2017). The thermal history predicted by QTQt using these parameters (Fig. 4B) satisfactorily reproduced all the thermochronological data available from the Brandberg Massif including the AHe dates older than AFT dates at high elevations (Fig. 4A; Raab et al., 2005; this study). Additionally, the model predicts a low geothermal gradient of ~15°C.km^{-1} in the Cenozoic consistent with present-day heat flux measurements and the region's geologic history over the last few tens of millions of years (e.g. 18-24°C .km^{-1}, Ballard et al., 1987; 26-30°C/km, Gholamrezaie et al., 2018).

Inversion of the Brandberg Massif age-elevation profile (AHe and AFT) indicates a rapid cooling at ~10°C/Myr after the emplacement of the Brandberg intrusion at high temperature (between 130 and 100 Ma; Fig. 4B). This rapid cooling is constrained by the Brandberg ^{39}Ar-^{40}Ar cooling dates at 132-130 Ma (Schmitt et al., 2000) and by AFT dates (Raab et al., 2005). The more recent cooling history (120-30°C) is well constrained by our AHe dates. From 100 to 65 Ma our data indicate a relatively quiet period with low cooling rate (Fig. 4B). From 65 to 35 Ma our data indicate a cooling episode with cooling rate ranging from 1°C/Myr to 2°C/Myr (Fig. 4B). According to the thermal modelling, the sample located at the highest elevation cooled more slowly than the one located at the lowest elevation (1°C/Myr vs. 2°C/Myr). From 35 Ma to present, the cooling rate is very low, less than 1°C/Myr indicating that the samples had reached near atmospheric temperatures (~20°C) by 35 Ma.

5. Discussion

5.1 Thermal and exhumation history of the Namibian Margin

The young AHe dates (66±5 to 30±2 Ma) obtained for the sample NAM14-08 (639 m) provide novel information on the recent cooling history of the Namibian margin as they are younger than any other thermochronological data published in this region (AFT; Haack et al. 1983; Raab et al., 2002; Raab et al., 2005; Brown et al. 2014). In agreement with these new AHe dates, thermal history modelling of AFT data and AHe dates evidences a recent exhumation phase between 65 and 35 Ma (Fig. 4B) that had not been identified before based only on AFT data (Raab et al., 2005). The AHe dates predicted by these thermal histories reproduce well the observed AHe dates (i.e., within uncertainty estimates). The predicted AFT dates and mean lengths are well reproduced (within uncertainties). We note that previous thermal history modelling by Raab et al. (2005)

317 was able to better reproduce the observed AFT dates. However, they were unable to
318 reproduce the track length measurements. We therefore favor our new modeled
319 thermal history (Fig. 4B) because it provide a better fit to the track length distributions,
320 an adequate fit to the AFT dates, and a good fit to the new AHe dates (Fig. 4A).
321
322 ***5.1.1 Escarpment retreat and uplift of the margin***
323 The thermal history obtained by inverse modelling of our new AHe dates combined with
324 published AFT data (Raab et al., 2005) suggests an early cooling phase between 130 and
325 100 Ma following the Brandberg intrusion emplacement and continental break-up in the
326 southern Atlantic (Fig. 4B). The initial cooling phase of the Brandberg Massif can be
327 explained by the combined effect of magmatic cooling of the intrusion, a change in
328 geothermal gradient after rifting and breakup, and erosion and uplift of the passive
329 margin following continental break-up at ~130 Ma (e.g. Brune et al., 2016; Baby et al.,
330 2018; Fig. 5A). However, based on available thermochronological dates and thermal
331 modelling it is not possible to assess the respective contribution of these three
332 processes in the Brandberg Massif. This mid-Cretaceous cooling phase has been
333 identified at many locations along the South African and South American Atlantic
334 margins and has been commonly attributed to denudation following continental break-
335 up (e.g. Brown, 1990; Brown et al., 1999; Gallagher and Brown, 1999; Cogné et al., 2012;
336 Brown, 2014; Wildman et al., 2016; 2018).
337
338 ***5.1.2 Influence of the Early Eocene Climatic Optimum: weathering and denudation?***
339 The AHe dates combined with AFT data constrain a second cooling phase in the
340 Brandberg Massif starting at ~65 Ma and ending at ~35 Ma (Fig. 4B). We interpret this
341 second cooling phase as a denudation phase. Taking a geothermal gradient of 20°C/km,

as suggested by the thermal modelling of the vertical profile and in agreement with Raab et al. (2005), this implies a denudation rate of 0.1 km/Myr and the removal of ~3 km of rocks during this denudation phase. However, the offshore sedimentation in the Walvis Basin, just to the west of the Brandberg Massif shows only a slight increase in sedimentation rates at that time with a deltaic wedge formation between 66 and 43.5 Ma (Aizawa et al., 2000; Baby, 2017). The volume of sediment deposited offshore since ~80 Ma (120±30 $\times 10^3$ km^3; Baby, 2017) is much smaller than the volume eroded onshore (325×10^3 km^3) as estimated from thermochronological data. This later estimate was obtained by extrapolating the cross sections given by Brown et al. (2014) representing the estimated depth of late Mesozoic denudation from the coast to the drainage divide to the present-day catchment of the Walvis Basin.

We postulate that the absence of offshore sedimentation is best explained by enhanced chemical weathering to cause denudation of the Namibian margin at that time. Indeed, the Brandberg Massif was partially emplaced in the Etendeka basaltic sequence (Schmitt et al., 2000). As basalts are one of the crystalline silicate rocks that are most easily weathered (Meybeck, 1987; Amiotte-Suchet and Probst, 1993) we suggest that the Etendeka basaltic sequence may have been intensively weathered and that only the highly weathered remnants have been physically eroded and transported (e.g. Guillocheau et al., 2018) producing a limited amount of sediments. It has been shown that rock types strongly influence the erosion pattern (Flowers and Ehlers, 2018), as seems to be the case here. In addition, intense weathering of a basaltic province has already been documented in other places such as India (Bonnet et al., 2016) and la Reunion (Dessert et al., 2003).

Alternatively, this discrepancy between the onshore and offshore records of erosion could be explained by the export of sediment out of the Walvis Basin by the northward

Benguela oceanic current. There is evidence for long (~1800 km) northward transport along the Atlantic margin from littoral sand derived from the Orange River in South Africa (Garzanti et al., 2018). However, the Walvis basin is bounded to the north by the Walvis Ridge and there is no evidence for a significant offshore sedimentary transport along the margin beyond the ridge.

The Cenozoic denudation phase that we have evidenced with the new AHe dates is synchronous with the Late Paleocene Thermal Maximum (59 Ma) and the Early Eocene Climatic Optimum (52-50 Ma) climatic anomalies (Zachos et al., 2001). First identified from marine cores, the Early Eocene Climatic Optimum is the warmest period of the Cenozoic; it correlates with increased atmospheric pCO_2 (Zachos et al., 2001) and major changes in marine (e.g., Zachos et al., 2001) and terrestrial records globally (e.g. Prasad, 1983; Greenwood and Wing, 1995; Hyland and Sheldon, 2013). In Namibia and southern western Africa only sparse climatic records are available. Based on fossil and sedimentary evidence including the presence of iron oxide nodules, Pickford and Senut, (1999) and Pickford et al. (2014) suggest a humid and warm climate for the Namibian margin with monsoonal episodes triggering enhanced weathering during the Early Eocene followed by an aridification of the climate starting in the middle Eocene (40 Ma; from pollens and fossil and sedimentary record; Scott et al., 2006; Pickford et al., 2014).

Weathering of silicate rocks (basalts) shows a strong dependence on temperature (Dessert et al., 2003). Several studies have identified increased weathering during the Early Eocene Climatic Optimum worldwide (e.g. Elliot Smith et al., 2008). In West Africa, a weathering phase has been identified between 60 and 50 Ma (Gunnell, 2003; Colin et al. 2005; Beauvais et al., 2008; Beauvais and Chardon, 2013). Along the Namibian margin remnants of the Etendeka flood basalts are sparse (Fig. 1A). In the Walvis Basin, located offshore from the Brandberg Massif, the occurrence of kaolinite as a major

392 secondary mineral in marine sediments at that time indicates a substantial weathering
393 period on the continent (Holtar and Forsberg, 2000).
394 As shown by Baby et al. (2018), a major unconformity developed between 81 and 70 Ma
395 in the offshore sedimentary basin indicating a significant relative sea level fall and a
396 bulging of the Namibian margin. We suggest that the erosion of that bulge was delayed
397 and only started about 10 Myrs after the uplift of the Namibian margin in response to an
398 intense and long-lasting weathering phase that started at ~65 Ma due to warmer and
399 wetter climatic conditions (Fig. 5).
400
401 ***5.1.3 Denudation of the Brandberg Massif and inselberg formation***
402 According to our thermal modelling, between 65 and 35 Ma the temperature difference
403 between the upper and lower samples decreased (Fig. 4B). The samples located in the
404 upper portion of the Brandberg Massif were cooling more slowly than those located at
405 lower elevations. This can be explained by higher erosion rates in the valleys and in the
406 areas surrounding the Brandberg Massif than along its crests and, consequently, by an
407 increase in topographic relief starting at 65 Ma. From 35 Ma to the present day the
408 estimated cooling rate is very low, i.e., less than 1°C/Myr. We propose that since 65 Ma
409 the area surrounding the Brandberg Massif recorded uniform denudation. This
410 phenomenon results in the incision of the main valleys of the Brandberg Massif while
411 the center of the massif is preserved therefore increasing local relief (Fig. 5). This Myr-
412 time-scale denudation pattern of the Brandberg is consistent with recent ^{10}Be erosion
413 rate obtained on several inselbergs in the region (Cockburn et al., 1999; Bierman and
414 Caffee, 2001; Matmon et al., 2013; Matmon et al., 2018). Indeed, based on inselbergs
415 morphology and ^{10}Be erosion rates it has been suggested that their formation and
416 erosion is driven by differential subsurface weathering of bedrock followed by base

level lowering and differential erosion (e.g. Twidale, 1964) and, at later stage, by cliff retreat, while the higher surfaces erode slowly (e.g. Cockburn et al., 1999). Since ~35 Ma the Brandberg has been exposed to atmospheric temperature (~20°C) and the cooling rates have been extremely low. These low erosion rates are consistent with the Late Eocene aridification of the area starting at 35 Ma (Scott et al., 2006; Pickford et al., 2014) and ^{10}Be erosion rates obtained in the Brandberg area for the Quaternary (~5 m.Myr^{-1}; Matmon et al., 2018).

In the case of the Brandberg Massif, or more broadly of other intrusions in this region, their emplacement at shallow depth (partly in the Etendeka Sequence) created a lithological contrast. Subsequently, preferential weathering of the Etendeka flood basalts might have favored denudation around the Early Cretaceous intrusions leading to the formation of inselbergs. The Proterozoic rock may also be more fractured than the Early Cretaceous intrusions forming the inselbergs, which could have had an impact on their weathering and thus on the differential erosion.

5.2 Comparison with the regional denudation history of the Namibian margin

Our thermal history suggests ~1 km of denudation from 65 Ma until present above the summit of the Brandberg Massif and ~3 km of denudation in the main valleys incised into the Brandberg Massif (Fig. 4b). The incision magnitude is in agreement with the amount of erosion recorded in the surrounding pediplains (Raab et al., 2005). However, the total amount of denudation (i.e., integrated over the last 130 Myr) is greater than the total amount of denudation in other areas along the margin (Brown et al., 2014). To explain the greater exhumation of the Brandberg area, some authors have proposed a Late Cenozoic reactivation of tectonic features in the Damara belt (Raab et al., 2002; Brown et al., 2014). We propose that this difference could also be due to the presence of

a thicker Etendeka volcanic sequence around the Brandberg volcanic complex that could have created a higher topography during rifting in the Brandberg region. In addition, the Damara shear zone hosting the Brandberg Massif is characterized by a lower effective elastic thickness than the surrounding African Atlantic margin (e.g. Pérez-Gussinyé et al., 2009), this could explain a different isostatic response to erosion seaward of the great escarpment and consequently a greater amount of erosion (e.g. Braun, 2018).

The timing of the cooling also differs slightly from some previous studies. Using the information given by both AFT and AHe on multiple samples in a vertical profile we were able to tightly constrain the thermal history of the Brandberg region from 130 Ma to 20 Ma. Based on our thermal history we suggest that the first cooling phase associated with continental break-up occurred at 130-100 Ma in accordance with previous estimates based on AFT data collected along the southern African margin (150-130 Ma; Wildman et al., 2015; 2016; Green et al., 2017). Tinker et al. (2008) also predict cooling at 140–120 Ma and relate it to denudation triggered by regional uplift above a buoyant mantle anomaly. The second cooling phase constrained by our data and modelling initiated at 65 Ma, which postdates the second major denudation phase that has been previously identified in several places along the margin from ~100-80 Ma to ~70-60 Ma (Haack, 1983; Raab et al., 2002; Brown et al., 2014). Our thermal history also differs from the single cooling episode (between 80 and 65 Ma) proposed by Raab et al. (2005) based on AFT data from the Brandberg (Refer to Fig 4b). Indeed, the AHe dates ranging from 66±5 to 30±2 Ma we obtained from the lowest elevation sample (NAM14-08) provide constraints on a more recent cooling phase between 65 and 35 Ma whereas the older thermochronological dates constrain the earlier cooling (Fig. 4 A, B). Recent advances in thermochronology in particular the better understanding of the effect of radiation damage on He trapping and reduced diffusivity in apatite (Gerin et al., 2017)

have allowed us to reconciles AFT data and AHe dates and to provide more robust constraints on the post break-up cooling history of the Brandberg area.

6. Conclusions

Along the Namibian margin low-temperature thermochronology provides information on denudation history that is only partially recorded in offshore sediments. Thermochronological data from the Brandberg Inselberg indicate two main cooling phases in this region since continental break-up at 130 Ma. We interpret the first one (between 130 and 100 Ma) to be related to post-rifting processes (cooling of the geothermal gradient/intrusion and escarpment erosion). We suggest that the second cooling phase from 65 to 35 Ma, is due to enhanced weathering and denudation caused by a change in precipitation rate and temperature during the Late Paleocene and Early Eocene Climatic Optimum warmer periods. We also suggest that the initiation of the Brandberg topography anomaly at 65 Ma lead the formation of the pediplains surrounding the Brandberg and the incision of the main valleys within the massif. Finally, the aridification of Namibia since 35 Ma resulted in the fossilization of the landscape and negligible denudation rates during the late Cenozoic.

Acknowledgements:

We thank the Franco-Namibian Cultural Centre and the Ambassade de France in Namibia for hosting our samples, the Geological Survey of Namibia and the National Heritage Council of Namibia for the authorizations and access to national parks. We acknowledge F. Coeur and F. Senebier as well as the GeoThermoChronology platform for the technical support during the sample processing at ISTerre, Grenoble. We acknowledge R. Brown for providing the AFT QTQt data files from Raab et al. (2005). (U-

Th-Sm)/He analysis have been funded by the ANR-12-BS06-0005 HeDiff project. We thank Guillaume Baby for discussions about Southern Africa geology and offshore basins.

References

Aizawa, M., B. Bluck, J. Cartwright, S. Milner, R. Swart, and J. Ward (2000), Constraints on the geomorphological evolution of Namibia from the offshore stratigraphic record. Communications of the Geological Survey of Namibia, 12, 337-346.

Amiotte-Suchet, P., and J. L. Probst (1993), Modelling of atmospheric CO2 consumption by chemical weathering of rocks: application to the Garonne, Congo and Amazon basins. Chemical Geology, 107(3-4), 205-210.

Geological map of Namibia (1980), 1: 2 000 000, Geological Survey of Namibia, Windhoek.

Baby, G. (2017), Mouvements verticaux des marges passives d'Afrique australe depuis 130 Ma, étude couplée : stratigraphie de bassin - analyse des formes du relief, Thèse de doctorat, Université de Rennes.

Baby, G., F. Guillocheau, J. Morin, J. Ressouche, C. Robin, O. Broucke, and M. Dall'Asta (2018), Post-rift stratigraphic evolution of the Atlantic margin of Namibia and South Africa: Implications for the vertical movements of the margin and the uplift history of the South African Plateau, Marine and Petroleum Geology, 97, 169–191, doi:10.1016/j.marpetgeo.2018.06.030.

Ballard, S., H. N. Pollack, and N. J. Skinner (1987), Terrestrial heat flow in Botswana and Namibia, Journal of Geophysical Research, Solid Earth, 92(B7), 6291–6300.

Beauvais, A., G. Ruffet, O. Hénocque, and F. Colin (2008), Chemical and physical erosion rhythms of the West African Cenozoic morphogenesis: The ^{39}Ar-^{40}Ar dating of supergene K-Mn oxides, Journal of Geophysical Research, Solid Earth, 113(F4), 124, doi:10.1093/petrology/5.3.359.

520 Beauvais, A., and D. Chardon (2013), Modes, tempo, and spatial variability of Cenozoic
521 cratonic denudation: The West African example, Geochem. Geophys. Geosyst., 14(5),
522 1590–1608, doi:10.1029/94JB00715.
523 Bierman, P. R., and M. Caffee (2001), Slow rates of rock surface erosion and sediment
524 production across the Namib Desert and escarpment, southern Africa, American
525 Journal of Science, 301, 326-358.
526 Bonnet, N. J., A. Beauvais, N. Arnaud, D. Chardon, M. Jayananda (2016), Cenozoic lateritic
527 weathering and erosion history of Peninsular India from $^{40}Ar/^{39}Ar$ dating of
528 supergene K–Mn oxides, Chem. Geol., 446, 33-53.
529 Braun, J. (2018), A review of numerical modeling studies of passive margin escarpments
530 leading to a new analytical expression for the rate of escarpment migration velocity,
531 Gondwana Research, 53(C), 209–224, doi:10.1016/j.gr.2017.04.012.
532 Brown, R. W., D. J. Rust, M. A. Summerfield, A. J. W. Gleadow, and M. C. J. De Wit (1990),
533 An Early Cretaceous phase of accelerated erosion on the south-western margin of
534 Africa: Evidence from apatite fission track analysis and the offshore sedimentary
535 record, Nuclear Tracks and Radiation Measurements, 17(3), 339-350.
536 Brown, R. W., R. Beucher, S. Roper, C. Persano, F. Stuart, and P. Fitzgerald (2013),
537 Natural age dispersion arising from the analysis of broken crystals. Part I: Theoretical
538 basis and implications for the apatite (U–Th)/He thermochronometer, Geochimica et
539 Cosmochimica Acta, 122(C), 478–497, doi:10.1016/j.gca.2013.05.041.
540 Brown, R., M. Summerfield, A. Gleadow, K. Gallagher, A. Carter, R. Beucher, and M.
541 Wildman (2014), Intracontinental deformation in southern Africa during the Late
542 Cretaceous, Journal of African Earth Sciences, 100(C), 20–41,
543 doi:10.1016/j.jafrearsci.2014.05.014.

544 Brune, S., S. E. Williams, N. P. Butterworth, and R. D. Müller (2016), Abrupt plate
545 accelerations shape rifted continental margins, Nature, 536(7615), 201–204,
546 doi:10.1038/nature18319.
547 Cockburn, H., M. A. Seidl, and M. A. Summerfield (1999), Quantifying denudation rates on
548 inselbergs in the central Namib Desert using in situ–produced cosmogenic ^{10}Be and
549 ^{26}Al, Geology, 27(5), 399-402.
550 Cockburn, H., R. W. Brown, and M. A. Summerfield (2000), Quantifying passive margin
551 denudation and landscape development using a combined fission-track
552 thermochronology and cosmogenic isotope analysis approach, Earth and Planetary
553 Science Letters, 179, 429-435.
554 Cogné, N., K. Gallagher, P.R. Cobbold, C. Riccomini and C. Gautheron (2012), Post-
555 breakup tectonics in southeast Brazil from thermochronological data and combined
556 inverse-forward thermal history modelling. Journal of Geophysical Research - Solid
557 Earth, 117.
558 Colin, F., A. Beauvais, G. Ruffet and O. Hénocque (2005), First 40Ar/39Ar geochronology
559 of lateritic manganiferous pisolites: Implications for the Palaeogene history of a West
560 African landscape. Earth and Planetary Science Letters, 238, 172-188.
561 Dauteuil, O., F. Deschamps, O. Bourgeois, A. Mocquet, and F. Guillocheau (2013), Post-
562 breakup evolution and palaeotopography of the North Namibian Margin during the
563 Meso-Cenozoic, Tectonophysics, 589(C), 103–115, doi:10.1016/j.tecto.2012.12.022.
564 Dessert, C., B. Dupré, J. Gaillardet, L. M. François, and C. J. Allègre (2003), Basalt
565 weathering laws and the impact of basalt weathering on the global carbon cycle,
566 Chemical Geology, 202(3-4), 257–273, doi:10.1016/j.chemgeo.2002.10.001.
567 Diehl, M. (1990). Geology, mineralogy, geochemistry and hydrothermal alteration of the
568 Brandberg alkaline complex, Namibia (No. 10). Geological Survey of Namibia.

569 Djimbi, D. M., C. Gautheron, J. Roques, L. Tassan-Got, C. Gerin, and E. Simoni (2015),
570 Impact of apatite chemical composition on (U-Th)/He thermochronometry: An
571 atomistic point of view, Geochimica et Cosmochimica Acta, 167, 162-176.
572 Elliot Smith, M., A. R. Carroll, and E. R. Mueller (2008), Elevated weathering rates in the
573 Rocky Mountains during the Early Eocene Climatic Optimum, Nature Geoscience,
574 1(6), 370–374, doi:10.1038/ngeo205.
575 Flowers, R. M., and S. A. Kelley (2011), Interpreting data dispersion and "inverted" dates
576 in apatite (U–Th)/He and fission-track datasets: An example from the US
577 midcontinent, Geochimica et Cosmochimica Acta, 75(18), 5169–5186,
578 doi:10.1016/j.gca.2011.06.016.
579 Flowers, R. M., R. A. Ketcham, D. L. Shuster, and K. A. Farley (2009), Apatite (U–Th)/He
580 thermochronometry using a radiation damage accumulation and annealing model,
581 Geochimica et Cosmochimica Acta, 73(8), 2347–2365, doi:10.1016/j.gca.2009.01.015.
582 Flowers, R. M., and T. A. Ehlers (2018), Rock erodibility and the interpretation of low-
583 temperature thermochronologic data, Earth and Planetary Science Letters, 482, 312–
584 323, doi:10.1016/j.epsl.2017.11.018.
585 Gallagher, K. (2012), Transdimensional inverse thermal history modeling for
586 quantitative thermochronology, Journal of Geophysical Research, Solid Earth,
587 117(B2), B02408, doi:10.1029/2011JB008825.
588 Gallagher, K., and R. Brown (1999), Denudation and uplift at passive margins: the record
589 on the Atlantic Margin of southern Africa, Philosophical Transactions of the Royal
590 Society A: Mathematical, Physical and Engineering Sciences, 357(1753), 835–859,
591 doi:10.1098/rsta.1999.0354.
592 Gallagher, K., R. Brown, and C. Johnson (1998), Fission track analysis and its applications
593 to geological problems, Annu. Rev. Earth Planet. Sci., 26(1), 519–572.

Garzanti, E., P. Dinis , P. Vermeesch , S. Andò, A. Hahn, J. Huvi, M. Limonta, M. Padoan, A. Resentini, M. Rittner, and G. Vezzoli, (2018), Sedimentary processes controlling ultralong cells of littoral transport: Placer formation and termination of the Orange sand highway in southern Angola, Sedimentology, 65, 431-460. doi:10.1111/sed.12387

Gautheron, C., J. Barbarand, R. A. Ketcham, L. Tassan-Got, P. van der Beek, M. Pagel, R. Pinna-Jamme, F. Couffignal, and M. Fialin (2013), Chemical Geology, Chemical Geology, 351(C), 257–267, doi:10.1016/j.chemgeo.2013.05.027.

Gautheron, C., L. Tassan-Got, J. Barbarand, and M. Pagel (2009), Effect of alpha-damage annealing on apatite (U–Th)/He thermochronology, Chemical Geology, 266(3), 157–170, doi:10.1016/j.chemgeo.2009.06.001.

Gerin, C., C. Gautheron, E. Oliviero, C. Bachelet, D. M. Djimbi, A.-M. Seydoux-Guillaume, L. Tassan-Got, P. Sarda, J. Roques, and F. Garrido (2017), Influence of vacancy damage on He diffusion in apatite, investigated at atomic to mineralogical scales, Geochimica et Cosmochimica Acta, 197, 87–103, doi:10.1016/j.gca.2016.10.018.

Gholamrezaie, E., M. Scheck-Wenderoth, J. Sippel, and M. R. Strecker (2018), Variability of the geothermal gradient across two differently aged magma-rich continental rifted margins of the Atlantic Ocean: the Southwest African and the Norwegian margins, Solid Earth, 9(1), 139–158, doi:10.5194/se-9-139-2018-supplement.

Gleadow, A. J. W., and P. G. Fitzgerald (1987), Uplift history and structure of the Transantarctic Mountains: new evidence from fission track dating of basement apatites in the Dry Valleys area, southern Victoria Land, Earth and Planetary Sciences Letters, 82, 1–14.

617 Gleadow, A. J. W., and R. W. Brown (2000), Fission track thermochronology and the long-
618 term denudational response to tectonics, in Geomorphology and global tectonics,
619 edited by M. J. Summerfield, pp. 57–75, Wiley, New York.
620 Glen, J. M. G., P. R. Renne, S. C. Milner, and R. S. Coe (1997), Magma flow inferred from
621 anisotropy of magnetic susceptibility in the coastal Paraná-Etendeka igneous
622 province: Evidence for rifting before flood volcanism, Geology, 25(12), 1131–1134.
623 Gradstein, F.M., J.G. Ogg, M.D. Schmitz, G.M. Ogg, 2012, The Geologic Time Scale 2012,
624 Elsevier, Oxford, United Kingdom (University of Oslo, Geological Museum, Oslo,
625 Norway).
626 Green, P. F. (1988), The relationship between track shortening and fission track age
627 reduction in apatite: combined influences of inherent instability, annealing
628 anisotropy, length bias and system calibration, Earth and Planetary Sciences Letters,
629 89, 335-352.
630 Green, P. F., I. R. Duddy, P. Japsen, J. M. Bonow, and J. A. Malan (2017), Post-breakup
631 burial and exhumation of the southern margin of Africa. Basin Research, 29(1), 96-
632 127.
633 Greenwood, D. R., and S. L. Wing (1995), Eocene continental climates and latitudinal
634 temperature gradients, Geology, 23(11), 1044–1048.
635 Guillocheau, F., B. Simon, G. Baby, P. Bessin, C. Robin, and O. Dauteuil (2018), Planation
636 surfaces as a record of mantle dynamics: The case example of Africa, Gondwana
637 Research, 53, 82-98, doi:10.1016/j.gr.2017.05.015.
638 Gunnell, Y. (2003), Radiometric ages of laterites and constraints on long-term
639 denudation rates in West Africa, Geology, 31, 131-134.

Haack, U. (1983), Reconstruction of the cooling history of the Damara orogen by correlation of radiometric ages with geography and altitude, in Intracontinental fold belts, edited by H. Martin and F. W. Eder, pp. 873–884, Berlin: Springer.

Holtar, E., and Forsberg, A. W. (2000), AAPG Memoir 73, Chapter 29: Postrift Development of the Walvis Basin, Namibia: Results from the Exploration Campaign in Quadrant 1911.

Hyland, E. G., and N. D. Sheldon (2013), Coupled CO2-climate response during the early Eocene climatic optimum, Palaeogeography, Palaeoclimatology, Palaeoecology, 369(C), 125–135, doi:10.1016/j.palaeo.2012.10.011.

Ketcham, R. A., A. Carter, R. A. Donelick, J. Barbarand, and A. J. Hurford (2007), Improved measurement of fission-track annealing in apatite using c-axis projection, American Mineralogist, 92(5-6), 789–798, doi:10.2138/am.2007.2280.

Ketcham, R. A., C. Gautheron, and L. Tassan-Got (2011), Accounting for long alpha-particle stopping distances in (U-Th-Sm)/He geochronology: Refinement of the baseline case, Geochimica et Cosmochimica Acta, 75(24), 7779–7791, doi:10.1016/j.gca.2011.10.011.

Matmon, A., A. Mushkin, Y. Enzel, T. Grodek, and A. Team (2013), Erosion of a granite inselberg, Gross Spitzkoppe, Namib Desert, Geomorphology, 201(C), 52–59, doi:10.1016/j.geomorph.2013.06.005.

Matmon, A., Y. Enzel, S. Vainer, T. Grodek, A. Mushkin, and A. Team (2018), Geomorphology, Geomorphology, 313, 1–16, doi:10.1016/j.geomorph.2018.04.008.

Meybeck, M., 1987. Global chemical weathering of surficial rocks estimated from river dissolved loads. Am. J. Sci. 287, 401 – 428.

Miller, R. M. (1983), The Pan-African Damara Orogen of South West Africa/Namibia, in Evolution of the Damara Orogen of South West Africa/Namibia.

665 Milner, S. C., A. R. Duncan, A. M. Whittingham, and A. Ewart (1995), Trans-Atlantic
666 correlation of eruptive sequences and individual silicic volcanic units within the
667 Parana-Etendeka igneous province, Journal of Volcanology and Geothermal Research,
668 69, 137–157.
669 Murray, K. E., D. A. Orme, and P. W. Reiners (2014), Effects of U–Th-rich grain boundary
670 phases on apatite helium ages, Chemical Geology, 390, 135-151.
671 Pérez-Gussinye, M., M. Metois, M. Fernández, J. Vergés, J. Fullea, and A. R. Lowry (2009),
672 Effective elastic thickness of Africa and its relationship to other proxies for
673 lithospheric structure and surface tectonics, Earth and Planetary Science Letters,
674 287(1-2), 152–167, doi:10.1016/j.epsl.2009.08.004.
675 Pickford, M. and B. Senut (1999), Geology and Palaeobiology of the Namib Desert
676 Southwest Africa, Mem., vol. 18, 155 pp., Geol. Surv. of Namibia, Windhoek, Namibia.
677 Pickford, M., B. Senut, H. Mocke, C. Mourer-Chauviré, J.-C. Rage, and P. Mein (2014),
678 Eocene aridity in southwestern Africa: timing of onset and biological consequences,
679 Transactions of the Royal Society of South Africa, 69(3), 139–144,
680 doi:10.1080/0035919X.2014.933452.
681 Raab, M. J., R. W. Brown, K. Gallagher, A. Carter, and K. Weber (2002), Late Cretaceous
682 reactivation of major crustal shear zones in northern Namibia: constraints from
683 apatite fission track analysis, Tectonophysics, 349, 75-92.
684 Raab, M. J., R. W. Brown, K. Gallagher, K. Weber, and A. J. W. Gleadow (2005),
685 Denudational and thermal history of the Early Cretaceous Brandberg and Okenyenya
686 igneous complexes on Namibia's Atlantic passive margin, Tectonics, 24(3),
687 doi:10.1007/BF00210550.
688 Recanati, A., C. Gautheron, J. Barbarand, Y. Missenard, R. Pinna-Jamme, L. Tassan-Got, A.
689 Carter, E. Douville, L. Bordier, M. Pagel, K. Gallagher (2017), Helium trapping in apatite

690 damage: Insights from (U-Th-Sm)/He dating of different granitoid lithologies, Chemical
691 Geology, 470, 116-131 doi:10.1016/j.chemgeo.2017.09.002.
692 Renne, P. R., J. M. Glen, S. C. Milner, and A. R. Duncan (1996), Age of Etendeka flood
693 volcanism and associated intrusions in southwestern Africa, Geology, 24(7), 659–662.
694 Prasad, G. (1983), A review of the early Tertiary bauxite event in South America, Africa
695 and India, Journal of African Earth Sciences, 1(3-4), 305–313, doi:10.1016/S0731-
696 7247(83)80015-9.
697 Rouby, D., S. Bonnet, F. Guillocheau, K. Gallagher, C. Robin, F. Biancotto, O. Dauteuil, and
698 J. Braun (2009), Sediment supply to the Orange sedimentary system over the last 150
699 My: An evaluation from sedimentation/denudation balance, 26(6), 782–794,
700 doi:10.1016/j.marpetgeo.2008.08.004.
701 Schmitt, A. K., R. Emmermann, and R. B. Trumbull (2000), Petrogenesis and 40Ar/39Ar
702 geochronology of the Brandberg Complex, Namibia: evidence for a major mantle
703 contribution in metaluminous and peralkaline granites, Journal of Petrology, 41(8),
704 1207–1239.
705 Scott, L., A. Cadman, and I. McMillan (2006), Early history of Cainozoic Asteraceae along
706 the Southern African west coast, Review of Palaeobotany and Palynology, 142(1-2),
707 47–52, doi:10.1016/j.revpalbo.2006.07.010.
708 Shuster, D. L., R. M. Flowers, and K. A. Farley (2006), The influence of natural radiation
709 damage on helium diffusion kinetics in apatite, Earth and Planetary Science Letters,
710 249(3-4), 148-161.
711 Stanley, J. R., R. M. Flowers, and D. R. Bell (2015), Erosion patterns and mantle sources of
712 topographic change across the southern African Plateau derived from the shallow and
713 deep records of kimberlites, Geochem. Geophys. Geosyst., 16(9), 3235–3256,
714 doi:10.1016/j.epsl.2011.10.041.

715 Stewart, K., S. Turner, S. Kelley, C. Hawkesworth, L. Kirstein, and M. Mantovani (1996), 3-
716 D, 40Ar-39Ar geochronology in the Parana continental flood basalt province, Earth
717 and Planetary Science Letters, 143, 95–109.
718 Tinker, J., M. de Wit, and R. Brown (2008), Mesozoic exhumation of the southern Cape,
719 South Africa, quantified using apatite fission track thermochronology,
720 Tectonophysics, 455(1-4), 77–93, doi:10.1016/j.tecto.2007.10.009.
721 Trumbull, R. B., T. Vietor, K. Hahne, R. Wackerle, and P. Ledru (2004), Aeromagnetic
722 mapping and reconnaissance geochemistry of the Early Cretaceous Henties Bay-Outjo
723 dike swarm, Etendeka Igneous Province, Namibia, Journal of African Earth Sciences,
724 40(1-2), 17–29, doi:10.1016/j.jafrearsci.2004.07.006.
725 Twidale, C. R. (1964), A contribution to the general theory of domed inselbergs, pp. 1–
726 30, Wiley.
727 Whipple, K. X. (2009), the influence of climate on the tectonic evolution of mountain
728 belts, Nature Geoscience, 2(10), 730–730, doi:10.1038/ngeo638.
729 Wildman, M., R. Brown, R. Watkins, A. Carter, A. Gleadow, and M. Summerfield, M.
730 (2015), Post break-up tectonic inversion across the southwestern cape of South
731 Africa: New insights from apatite and zircon fission track thermochronometry,
732 Tectonophysics, 654, 30-55.
733 Wildman, M., R. Brown, R. Beucher, C. Persano, F. Stuart, K. Gallagher, J. Schwanethal,
734 and A. Carter (2016), The chronology and tectonic style of landscape evolution along
735 the elevated Atlantic continental margin of South Africa resolved by joint apatite
736 fission track and (U-Th-Sm)/He thermochronology, Tectonics, 35, 511–545,
737 doi:10.1002/(ISSN)1944-9194.
738 Wildman, M., R. Brown, C. Persano, R. Beucher, F. M. Stuart, V. Mackintosh, K. Gallagher,
739 J. Schwanethal, and A. Carter (2017), Contrasting Mesozoic evolution across the

740 boundary between on and off craton regions of the South African plateau inferred
741 from apatite fission track and (U-Th-Sm)/He thermochronology, Journal of
742 Geophysical Research, Solid Earth, 122(154), 1517–1547,
743 doi:10.1126/science.1059412.
744 Wildman, M., D. Webster, R. Brown, D. Chardon, D. Rouby, J. Ye, D. Huyghe, and M.
745 Dall'Asta (2018), Long-term evolution of the West African transform margin:
746 estimates of denudation from Benin using apatite thermochronology, Journal of the
747 Geological, Society, 1–18, doi:10.6084/m9.figshare.c.4220804.
748 Wildman, M., N. Cogné, and R. Beucher (2019), Fission-track thermochronology applied
749 to the evolution of passive continental margins, in Fission-Track Thermochronology
750 and its Application to Geology, Springer, Cham, 351-371.
751 Willett, S. D. (1999), Orogeny and orography: The effects of erosion on the structure of
752 mountain belts, Journal of Geophysical Research: Solid Earth (1978–2012), 104(B12),
753 28957–28981.
754 Zachos, J. C., M. Pagani, L. Sloan, E. Thomas, and K. Billups (2001), Trends, Rhythms, and
755 Aberrations in Global Climate 65 Ma to Present, Science, 292, 1–9.
756 Zeitler, P. K., E. Enkelmann, J. B. Thomas, E. B. Watson, L. D. Ancuta, and B. D. Idleman
757 (2017), Solubility and trapping of helium in apatite, Geochimica et Cosmochimica
758 Acta, 209, 1–8, doi:10.1016/j.gca.2017.03.041.

FIG 1: (A) Geological map of Namibian margin showing the Early Cretaceous intrusions, major tectonic lineaments, available AFT data and our sampling sites for AHe dating (the inset shows the location of the study area within Africa, geological map is modified from the Geological Survey of Namibia, 1980). (B) Topographic cross-section of the great escarpment in Namibia including the Brandberg Inselberg. (C) Geological map of the Brandberg Inselberg showing the location of the Hungorob and Tsisab Valleys (respectively indicated by HV and TV), AFT (Raab et al., 2005) and AHe (this study) sample locations (modified from Schmitt et al., 2000).

FIG 2: AHe data for the Brandberg area. (A) Individual grain non corrected AHe date against sample elevation, the orange pastel point indicates a grain that might be impacted by implantation. (B) Individual grain non corrected AHe date against eU.

FIG 3: (A, C) Age elevation profiles showing AFT dates, mean track length (TL) and AHe dates (non corrected AHe dates) and predicted dates for the thermal histories using Gautheron et al. (2009) and Flowers et al. (2009) radiation damage models. (B, D) Predicted thermal histories using Gautheron et al. (2009) and Flowers et al. (2009) radiation damage models. Each line represents the thermal history of a sample; the red line represents path of lowest elevation sample and blue line the highest one, pastel shading represents uncertainties.

FIG 4: (A) Brandberg age elevation profile showing AFT dates, mean track length (TL) and AHe dates (non corrected AHe dates) and predicted dates for the preferred thermal history using Gerin et al. (2017) radiation damage model. (B) Thermal history. Each line represents the thermal history of a sample; the red line represents path of lowest

784 elevation sample and blue line the highest one, red and blue pastel shadings represent
785 uncertainties. The thermal history proposed by Raab et al. (2005) based on AFT data is
786 indicated in green for reference. (C) Sediments volumes in the Walvis Bay (Baby, 2017).
787 (D) Regional climate inferred from local proxies (Pickford and Senut, 1999; Scott et al.,
788 2006; Pickford et al., 2014). (E) Global deep-sea oxygen and carbon isotope records
789 based on data compiled from DSDP and ODP sites and inferred temperature anomalies
790 (Zachos et al., 2001). The late Paleocene Thermal Maximum (referred as LPTM on the
791 figure) and the Early Eocene Climatic Optimum (referred as EECO) climatic aberrations
792 are highlighted in red. (F) Geodynamic events (e.g. Brune et al., 2016; Schmitt et al.,
793 2000; Baby et al., 2018;.
794
795 FIG 5: Reconstitution of the topographic evolution and denudation history of the
796 Brandberg. For each time step, the AHe partial retention zone is highlighted in orange,
797 the eroded material is indicated by pastel colors and the location of the AHe samples is
798 indicated by the white triangles. (A) 130 Ma: Rifting, emplacement of Etendeka volcanic
799 sequence and Brandberg intrusion. (B) 130-100 Ma: Post-rift decrease of the geothermal
800 gradient, magmatic cooling and erosion of the margin. (C) 100-65 Ma: Regional uplift of
801 the Namibian margin. (D) 65-35 Ma: Paleocene warming, starting at that time the humid
802 and warm climate in Namibia might have enhanced weathering and denudation. (E) 35-
803 0 Ma: Eocene aridification decrease of the erosion rates and stabilization of the
804 landscape.
805

Figure 1

Click here to download high resolution image

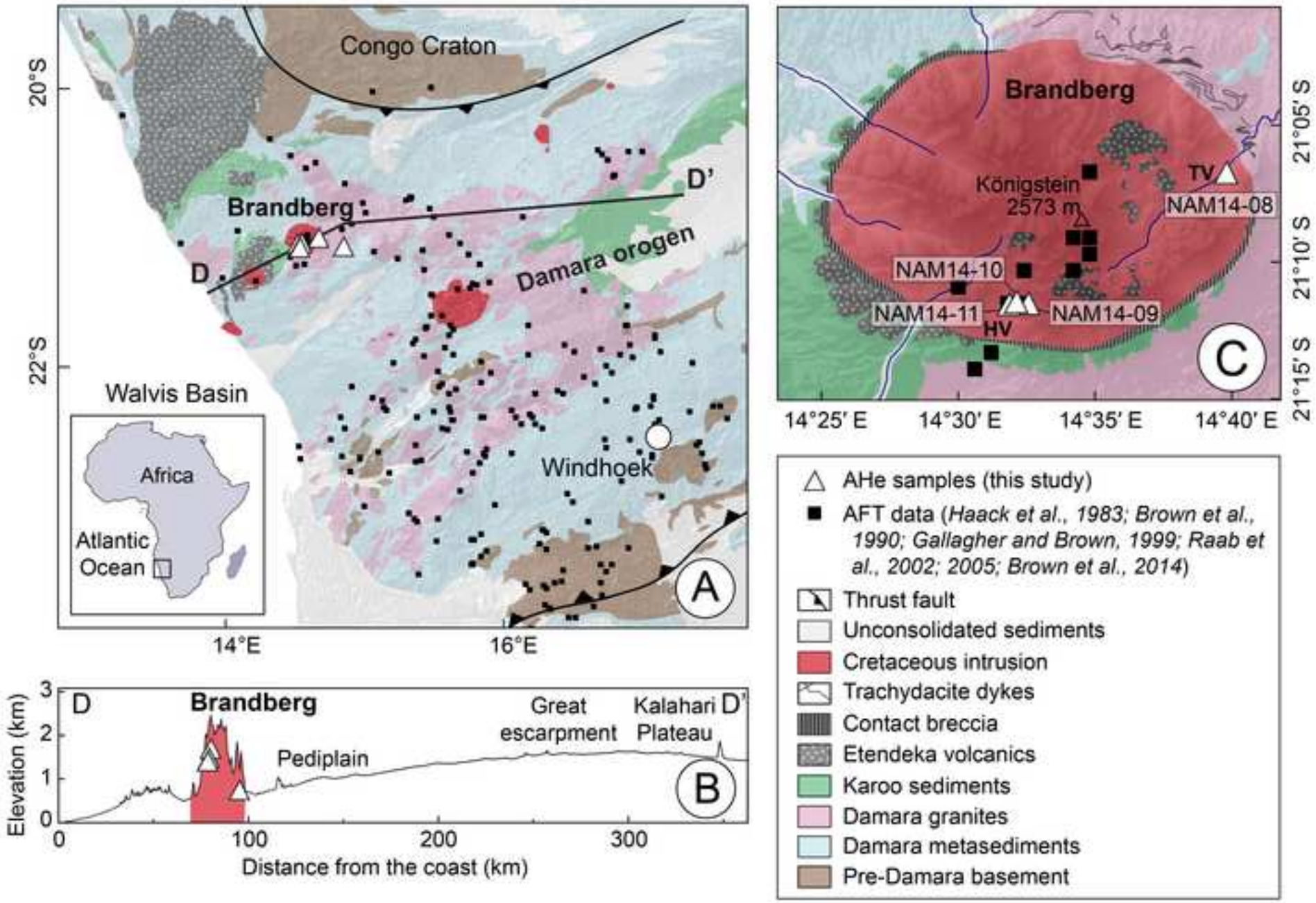

Figure 2

Click here to download high resolution image

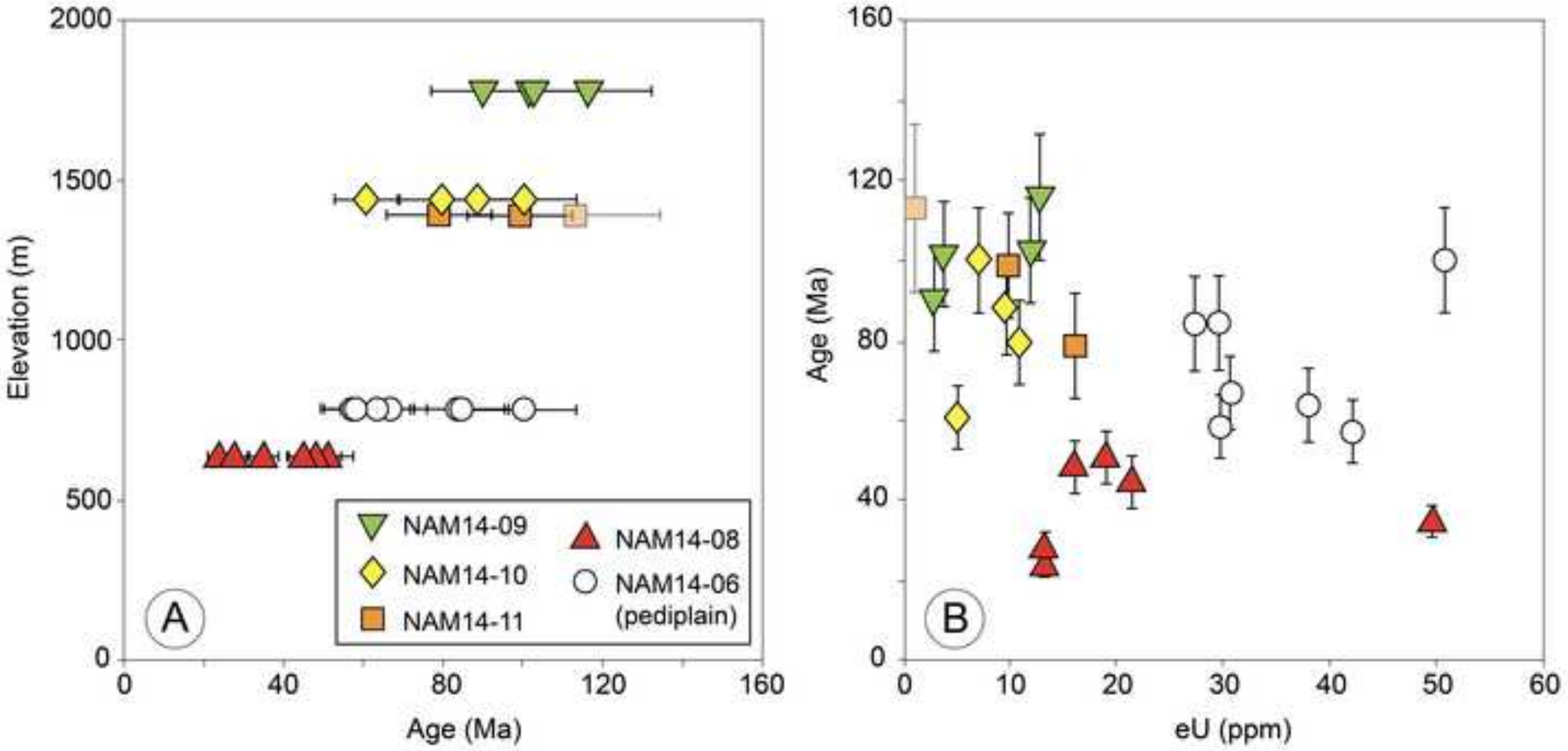

Figure 3

Click here to download high resolution image

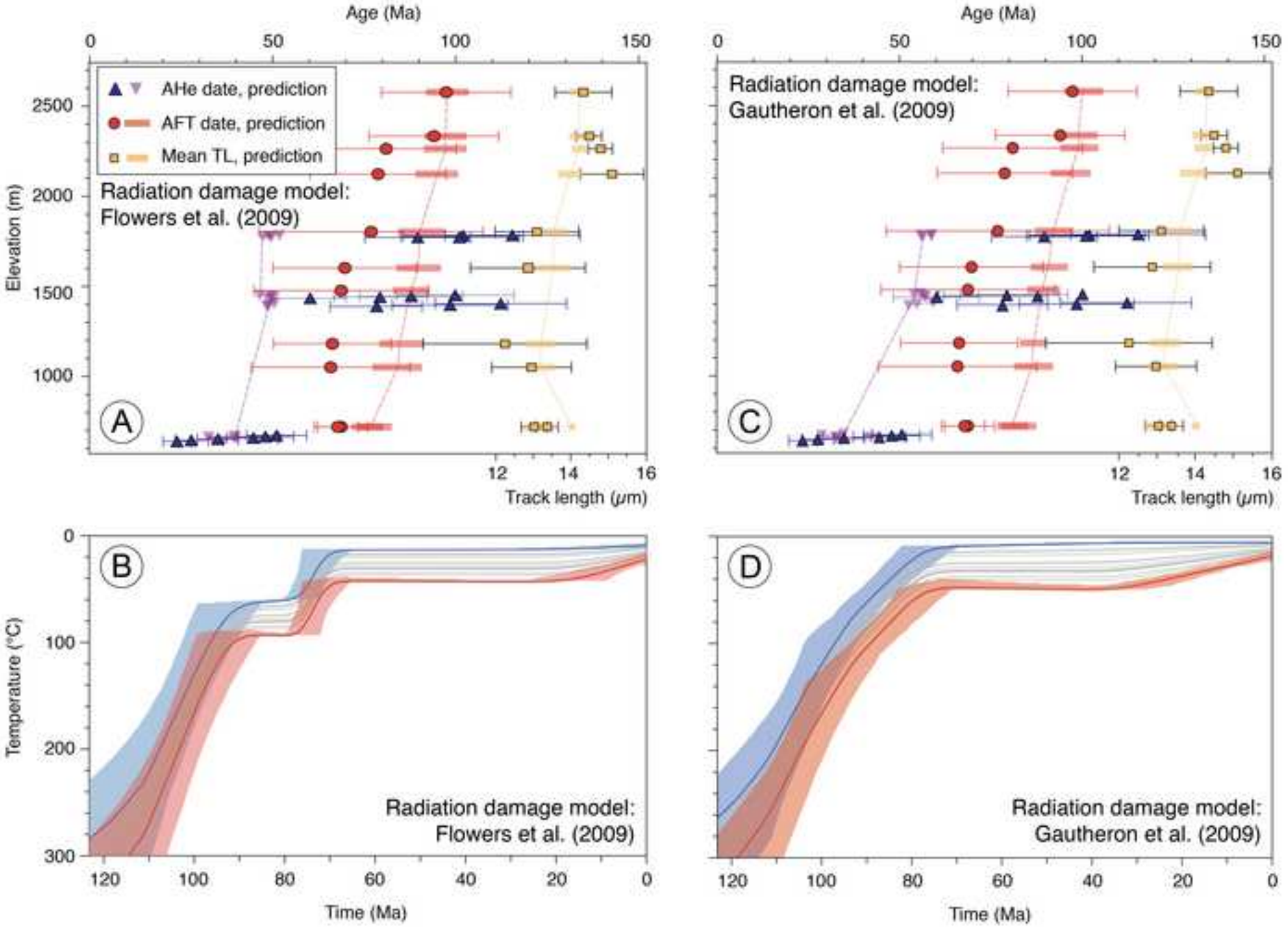

Figure 4

Click here to download high resolution image

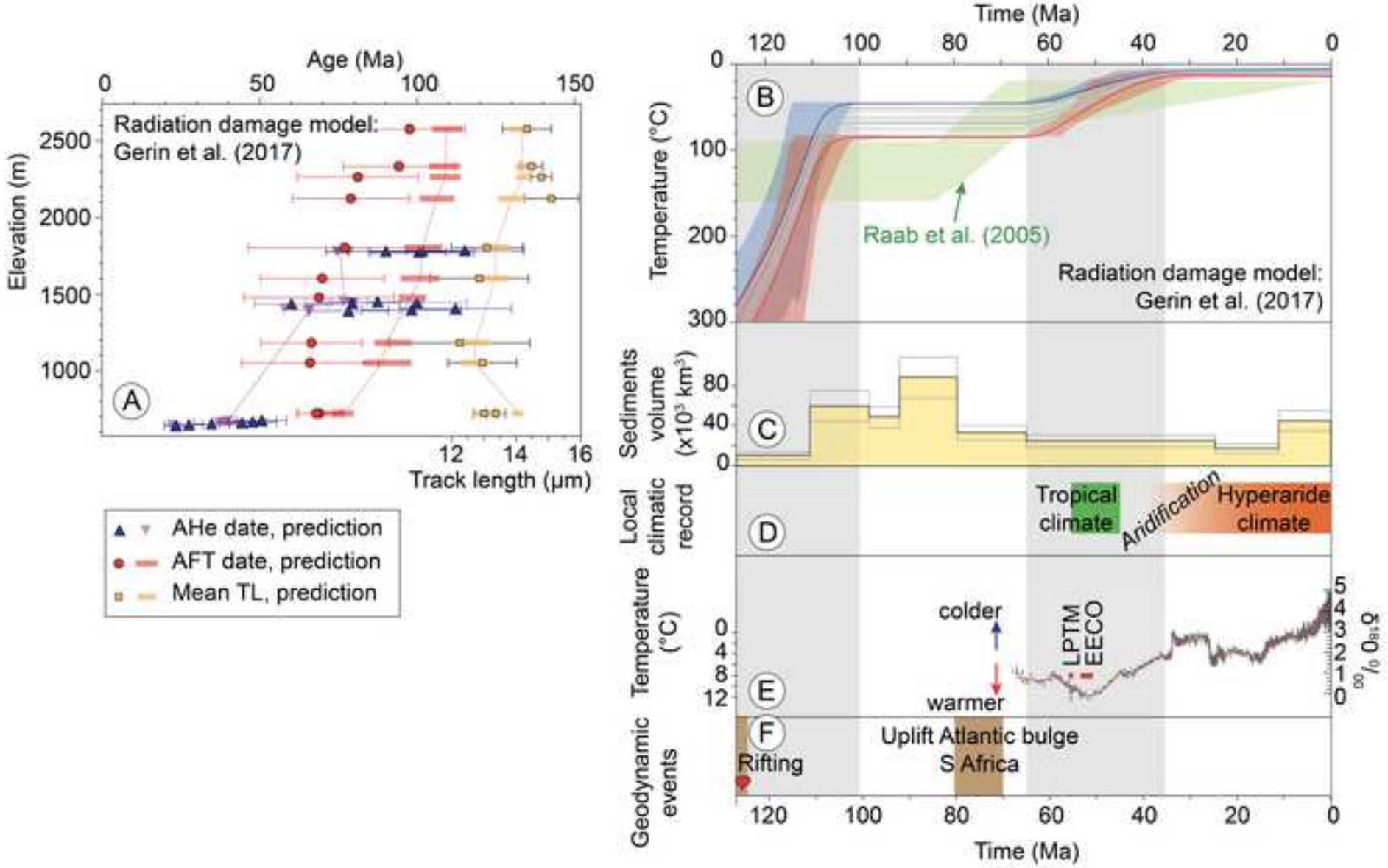

Figure 5

Click here to download high resolution image

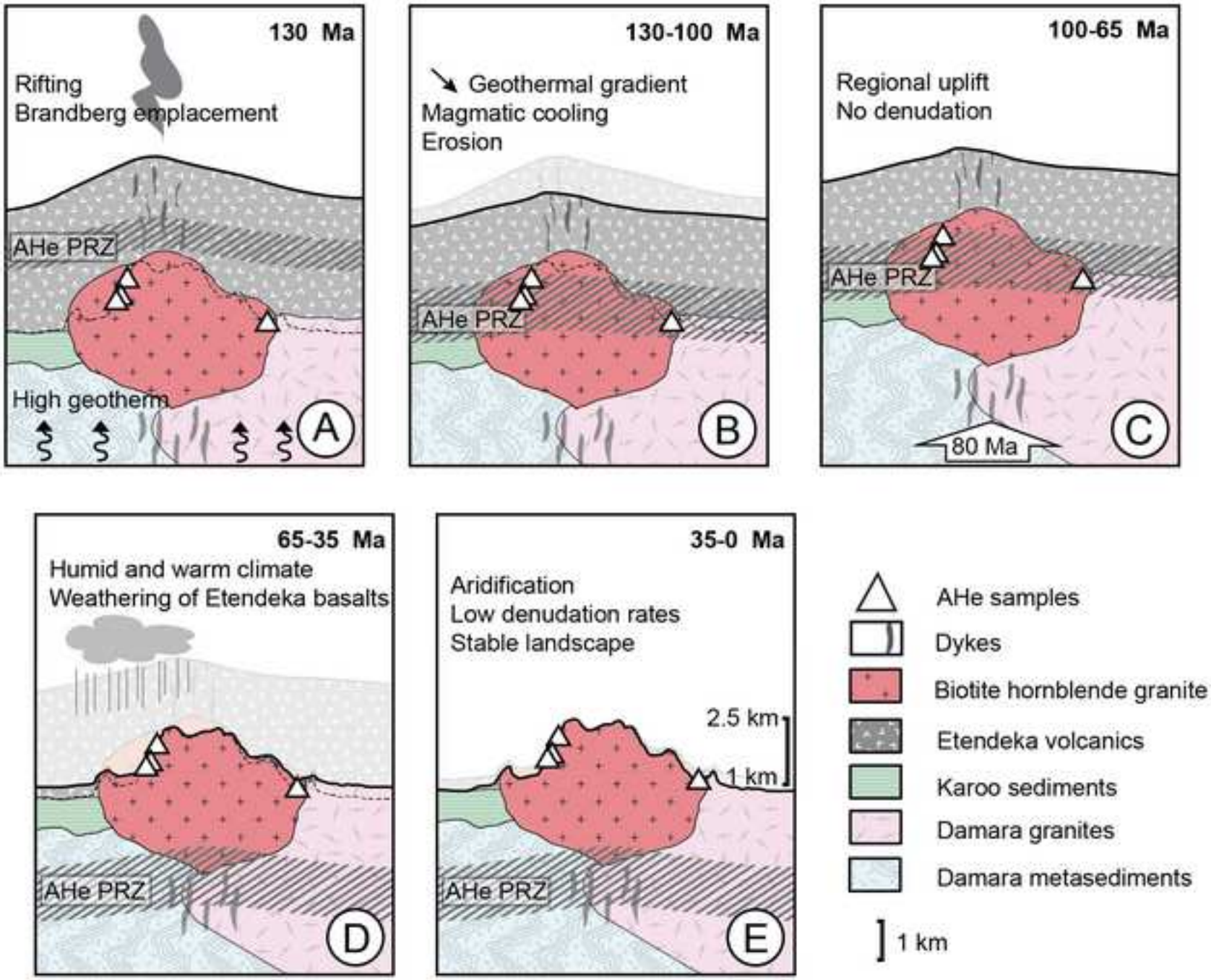

Table

Click here to download Table: Tab data AHe.pdf

TABLE 1: APATITE (U-Th-Sm)/He SINGLE-GRAIN AGES FROM THE BRANDBERG INSELBERG AND PEDIPLAIN (NAMIBIA)

Sample	Rock	Location*		Elevation	Weight	Rs†	FT§	4He	U	Th	Sm	eU	Th/U	AHe age	Corrected
		Latitude (°N)	Longitude (°W)	(m)	(µg)			(nccSTP/g)	(ppm)	(ppm)	(ppm)	(ppm)#		(Ma)	AHe age ± error (Ma)**
Pediplain															
NAM14-6A	granite	14,8451944	-21,169222	780	4,0	51,1	0,77	303159	23,5	24,7	174,9	30	1,1	84,9	111.0 ± 8.9
NAM14-6D	granite	14,8451944	-21,169222	780	4,0	55,6	0,81	248738	23,0	31,9	152,1	31	1,4	67,0	83.2 ± 6.7
NAM14-6F	granite	14,8451944	-21,169222	780	2,6	46,1	0,75	292020	31,2	27,7	205,8	38	0,9	63,6	84.7 ± 6.8
NAM14-6G	granite	14,8451944	-21,169222	780	3,6	51,8	0,78	277302	19,2	33,3	174,7	27	1,7	83,9	107.6 ± 8.6
NAM14-6I	granite	14,8451944	-21,169222	780	3,0	53,4	0,79	613209	37,2	55,6	240,4	51	1,5	100,2	127.6 ± 10.2
NAM14-6K	granite	14,8451944	-21,169222	780	2,2	47,8	0,75	290618	31,2	44,7	265,9	42	1,4	57,0	75.9 ± 6.1
NAM140-6bA	granite	14,8451944	-21,169222	780	5,9	60,5	0,81	213116	23,2	27,3	635,7	30	1,2	58,0	71.7 ± 5.7
Brandberg Inselberg															
NAM14-09A	granite	14,5426667	-21,190444	1769	2,9	49,6	0,77	147310	6,2	22,5	287,6	12	3,6	102,6	132.7 ± 10.6
NAM14-09B	granite	14,5426667	-21,190444	1769	4,4	57,5	0,81	45827	1,7	7,8	167,7	4	4,7	101,6	124.8 ± 10.0
NAM14-09bA	granite	14,5426667	-21,190444	1769	4,2	55,6	0,77	179269	7,0	23,4	157,1	13	3,3	116,2	150.8 ± 12.1
NAM14-09bB	granite	14,5426667	-21,190444	1769	2,8	50,8	0,76	32120	2,6	0,7	111,3	3	0,3	90,1	119.0 ± 9.5
NAM14-10bA	granite	14,5350556	-21,189306	1433	4,0	54,8	0,77	87993	4,4	10,7	243,3	7	2,4	100,7	131.1 ± 10.5
NAM14-10A	granite	14,5350556	-21,189306	1433	3,9	58,0	0,79	101969	6,0	13,8	182,6	10	2,3	88,4	111,6 ± 8.9
NAM14-10G	granite	14,5350556	-21,189306	1433	5,3	64,4	0,82	36620	2,3	11,3	7,1	5	4,9	60,7	74.2 ± 5.9
NAM14-10H	granite	14,5350556	-21,189306	1433	5,7	60,0	0,81	104446	5,7	21,4	85,5	11	3,8	79,9	99.1 ± 7.9
NAM14-11A	granite	14,5317222	-21,189917	1387	4,0	56,3	0,81	459245	12,0	43,6	259,4	23	3,6	167,7	207.1 ± 16.6††e
NAM14-11B	granite	14,5317222	-21,189917	1387	3,1	51,5	0,81	153691	10,6	21,9	276,0	16	2,1	78,7	97.5 ± 10.1
NAM14-11C	granite	14,5317222	-21,189917	1387	3,7	57,3	0,79	118983	5,6	16,9	248,0	10	3,0	99,1	126.1 ± 10.1
NAM14-11F	granite	14,5317222	-21,189917	1387	8,6	71,7	0,81	16082	0,7	1,6	86,6	1	2,2	113,1	140.3 ± 11.2
NAM14-08B	granite	14,6635	-21,110472	639	3,5	53,1	0,80	43815	8,5	18,6	216,1	13	2,2	27,6	34.6 ± 2.8
NAM14-08C	granite	14,6635	-21,110472	639	2,1	46,0	0,73	93645	9,4	26,7	354,8	16	2,8	48,0	65.9 ± 5.3
NAM14-08D	granite	14,6635	-21,110472	639	3,2	54,5	0,78	117194	10,3	35,3	327,6	19	3,4	50,9	65.3 ± 5.2
NAM-14-08bA	granite	14,6635	-21,110472	639	3,7	56,8	0,79	37978	6,7	27,3	167,5	13	4,1	23,6	30.0 ± 2.4
NAM14-08bC	granite	14,6635	-21,110472	639	2,7	50,9	0,76	115134	11,3	41,3	247,9	21	3,7	44,7	58.6 ± 4.7
NAM14-08bF	granite	14,6635	-21,110472	639	4,5	58,8	0,79	208337	30,7	78,3	177,4	50	2,5	34,9	44.3 ± 3.5

Notes:

*Longitude and latitude coordinates are given in WGS 84 (degrees).

†Rs is the sphere equivalent radius of hexagonal crystal with the same surface/volume ratio.

§FT is the geometric correction factor for age calculation.

#eU is the effective uranium concentration.

**Corrected age is the age corrected by the grain geometry and ejection factor FT (Gautheron and Tassan-Got, 2010; Ketcham et al., 2011), error at 1σ.

††e indicates that the age was rejected for the modelling (possible inclusion).

Supplementary material for online publication only

Click here to download Supplementary material for online publication only: Supplements Namibia_CG.docx